International Journal of Applied Power Engineering (IJAPE)
Vol. 15, No. 3, September 2026, pp. 1299~1313
ISSN: 2252-8792, DOI: 10.11591/ijape.v15.i3.pp1299-1313 ❒ 1299

MPPT control of a PV-battery system using a gain-scheduled adaptive PI controller and dual active bridge converter

Khalid Sabhi, Mohamed Talea, Hicham Bahri
Department of Physics, Laboratory of Information Processing, Faculty of Sciences Ben M'Sick,
Hassan II University of Casablanca, Casablanca, Morocco

Article Info

Article history:

Received Aug 5, 2025
Revised Jun 19, 2026
Accepted Aug 15, 2026

Keywords:

Dual active bridge
Gain-scheduled PI controller
Maximum power point tracking
Photovoltaic panel
Single phase shift modulation

ABSTRACT

Standalone photovoltaic-battery systems face significant challenges in maintaining optimal power extraction under rapidly varying irradiance conditions. Conventional MPPT controllers based on fixed-gain PI approaches suffer from poor dynamic response, oscillations around the maximum power point, and inability to adapt to the nonlinear behavior of dual active bridge (DAB) converters across different operating points. To address these limitations, this work proposes an innovative adaptive control strategy for maximum power point tracking (MPPT) in a stand-alone photovoltaic-battery system connected via a DAB converter. The gain-scheduled PI controller is recalculated at each 1 µs sample by local linearization of the complete nonlinear model of the PV-DAB-battery system, with explicit compensation for measurable disturbances (derived from irradiance G and temperature T). MATLAB/Simulink simulations under realistic irradiance profiles (slow ramps simulating the passage of clouds) demonstrate a clear superiority over a classic PI with fixed gains: ultra-fast response (approximately 1 ms), total absence of oscillations and overshoots, and strict maintenance of a constant second-order dynamic over the entire operating range. To our knowledge, this gain-scheduled analytical approach with explicit perturbation compensation has never before been applied to DAB topology in PV-battery systems. It is distinguished by its ease of implementation, low computational load, and robustness without the need for complex observers. This work lays the groundwork for future experimental validation and extensions to multi-source hybrid systems.

Corresponding Author:

Khalid Sabhi
Department of Physics, Laboratory of Information Processing, Faculty of Sciences Ben M'Sick
Hassan II University of Casablanca
Casablanca, Morocco
Email: sabhi.khalid.imt@gmail.com

1. INTRODUCTION

Standalone photovoltaic (PV-battery) systems are essential for powering off-grid locations. Their performance depends on two main factors: the PV-battery combination and the adopted control strategy. PV panels undergo rapid variations in solar irradiance G [1], [2], which can cause current oscillations, inaccurate tracking of the maximum power point (MPP), and a reduction in overall efficiency [3]-[6]. Furthermore, conventional fixed-gain controllers do not adapt to system nonlinearities, leading to instability and inefficiency [7]-[9]. The review showed that the most common PV-battery architectures are based on a DC bus coupled with a boost converter that operates by varying the duty cycle [10]-[12]. This structure is simple, but the review highlighted several limitations: the dependence on the duty cycle directly modifies the constraints on the inductance and capacitors, making the sizing of passive components sensitive to variations in irradiance and load conditions.

A comprehensive review of the literature confirmed the prevalent application of the traditional proportional-integral (PI) controller for MPP tracking and the management of buck/boost converters [13], [14]. Nevertheless, the results demonstrated that this empirically tuned controller remained strictly linear. This characteristic results in oscillations around the MPP, limited robustness, and an inability to compensate for nonlinear dynamics of the PV converter. Although only unidirectional power flow is required, the dual active bridge (DAB) converter was selected because it controls the transferred power precisely through phase-shift while maintaining a fixed switching frequency and 50% duty cycle, thus optimizing the design of passive components.

Fixed-gain PI controllers cause oscillations or loss of tracking of the maximum power point during realistic gradual changes in irradiance G (slow slopes simulating cloud passage), whereas most existing strategies are only validated on abrupt G steps, and real-world dynamics are continuous and significantly alter the small-signal behavior at each operating point [15], [16]. Moreover, the pronounced nonlinearity of the photovoltaic (PV) generator, coupled with the bilinear characteristics of power transfer in the DAB, renders the system performance, specifically in terms of speed and damping, highly contingent on the operating point when utilizing a conventional proportional-integral PI controller. Very few studies have proposed a simple and systematic recalculation of the gains in real time with explicit compensation for measurable disturbances (G and T slopes) without a complex observer or computationally intensive analysis [17]-[20].

This study proposed a gain-scheduled PI with explicit perturbation compensation, recalculating gains K_p and K_i every 1us by fast local linearization of the nonlinear PV-DAB-battery model and injecting a correction term based on the measured derivatives of G and T. As depicted in Figure 1, this control, which is novel in the literature for this topology [21], [22], ensures strictly second-order dynamics, characterized by a constant response time and overshoot across the entire operating range. It effectively eliminates oscillations and tracking losses of the reference current during realistic progressive irradiance variations, such as continuous slopes that simulate cloud passage. Furthermore, it achieves these outcomes without the need for a complex observer or excessive computational resources, thereby offering a straightforward and robust solution that can be directly implemented in DAB-based PV-battery systems [23], [24].

The remainder of this manuscript is structured as follows: Section 2 establishes the complete nonlinear mathematical model of the PV-DAB-battery subsystem and its local linearization at each instant; Section 3 details the design of the PI with programmed gains, the analytical calculation of the gains K_p and K_i as a function of the instantaneous operating point, and the addition of the compensation term for the measured disturbances; Section 4 presents the results of the MATLAB/Simulink simulations under realistic irradiance profiles (continuous slopes), compares the performance with that of a conventional PI with fixed gains, and demonstrates the perfect constancy of the second-order dynamics as well as the complete elimination of oscillations; finally, Section 5 concludes with the contributions of this study, discusses the remaining limitations (actual measurement uncertainties, real-time implementation), and outlines the experimental perspectives and possible extensions.

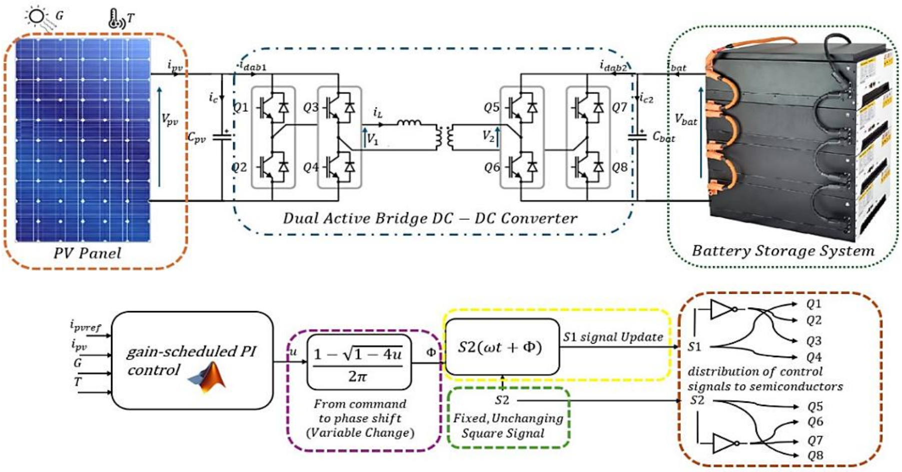

Figure 1. Block diagram of the system and control

2. METHOD

2.1. Simulation platform and validation protocol

All the results presented in this article were obtained through simulations using MATLAB/Simulink R2023b (without Simscape Electrical) with a fixed-step solver of $1 \times 10^{-6} s$ (fixed-step, auto solver). The DAB converter was modeled in the switched state (switching model) for maximum accuracy [25]. The battery is represented by the standard Simulink "battery" block (lithium-ion, nominal voltage 500 V, capacity 200 Ah) [26], [27]. The variations in sunlight were generated according to realistic profiles inspired by the EN 50530 standard (ramps of 10–50 W/m²/s, steps 100–1000 W/m² and cloud passages of a few seconds).

2.2. System modeling and sizing

2.2.1. Photovoltaic source

The simulated photovoltaic array delivered a peak power of 64 kW under STC conditions (G = 1000 W/m², T = 25 °C). It consists of 15 parallel branches (Np = 15), each comprising 20 modules in series (Ns = 20), and each module is composed of 60 cells in series (Nc = 60). The electrical model used is the classic single-diode model with series and parallel resistors (single-diode model [28]), which has been widely validated in the literature. The model parameters, which were determined to accurately reproduce the manufacturer's characteristic points at different levels of solar irradiance and temperature, are listed in Table 1.

Accurate panel modeling is essential for monitoring MPPs and managing environmental variations. An equivalent diagram (Figure 2) based on the single diode model captures the nonlinear behaviors, current generator (i_{ph}) for photocurrent, parallel diode (i_d) for p-n junction and parasitic resistances for imperfections. Respectively R_{sh} represents defect losses (short circuits, impurities), and R_s resistive losses (metal contacts, semiconductor layers).

The complete structure, shown in Figure 3, adapts the voltage and current to the requirements of the DAB-battery system. The total panel current i_{pv}, photocurrent ti_{ph}, and diode current i_d are expressed as follows:

$$i_{pv} = N_p i_{ph} - N_p i_d - i_{Rsh} \tag{1}$$

$$i_{ph} = i_{ph\_}0 \frac{G}{1000}\left(1 + \beta_T (T - 25)\right) \tag{2}$$

$$i_d = i_0 \left(e^{\left(\frac{qV_d}{nkT}\right)} - 1\right) \tag{3}$$

where $q = 1.602 * 10^{-19} C$ (elementary charge), $n = 0.98119$ (diode ideality factor, ideal junction deviations), and $k = 1.381 * 10^{-23} J/K$(Boltzmann constant, thermal energy). The diode voltage V_d, shunt current i_{rsh}, representing the losses in R_{sh}, are:

$$V_d = \frac{V_{pv}}{N_s N_c} + \frac{R_s i_{pv}}{N_p N_c} \tag{4}$$

$$i_{rsh} = \frac{N_p V_{pv}}{N_s R_{sh}} + \frac{R_s i_{pv}}{R_{sh}} \tag{5}$$

where V_{pv} is the panel voltage, R_s is the series resistance, and N_s and N_c are the number of cells in series and total.

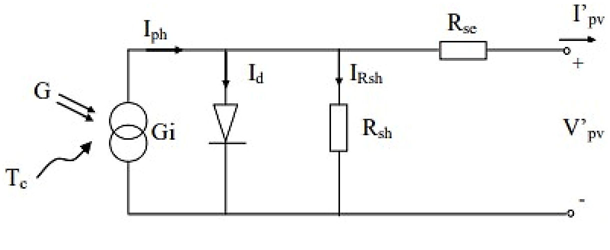

Figure 2. Equivalent single-diode circuit of a PV cell, showing the photocurrent source iph, diode, series resistance Rs, and shunt resistance Rsh

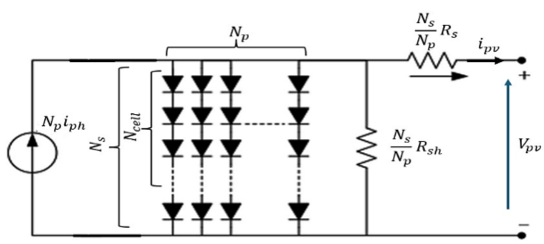

Figure 3. Equivalent diagram of the PV panel used

Table 1. Photovoltaic model parameters at STC (1000 W/m², 25 °C)

Parameter	Value
Light-generated current IL	7.8654 A
Diode saturation current I_0	2.9273×10^{-10} A
Diode ideality factor a	0.98119
Series resistance Rs (per module)	0.39381 Ω
Shunt resistance Rsh (per module)	313.0553 Ω

To validate the accuracy of the adopted one-diode model, the simulated I–V characteristics are compared with the manufacturer’s datasheet of the photovoltaic module A10Green Technology A10J-M60-220. The model parameters are adjusted to match the key electrical specifications at standard test conditions (STC), including open-circuit voltage, short-circuit current, and maximum power point. As shown in Figure 4, the obtained I–V curves under different irradiance levels and cell temperatures demonstrate a good agreement with the expected behavior of the module, confirming the validity of the adopted model.

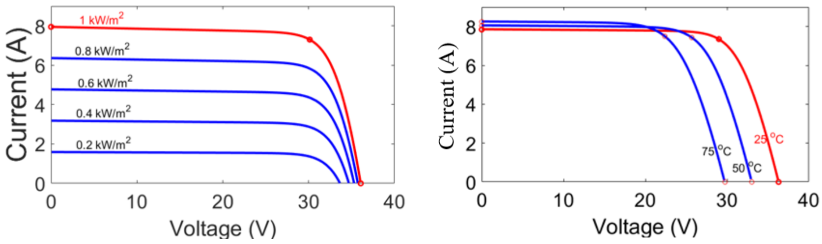

Figure 4. Current–voltage characteristics of the photovoltaic module A10Green Technology A10J-M60-220: (a) under various irradiance levels and (b) under different cell temperatures

2.2.2. Average input current analysis for DAB converter

The photovoltaic array is interfaced with the battery via a DAB converter (Figure 1) with the following simulation parameters:

- Leakage inductance (referred to the PV side): L = 50 µH
- Switching frequency: fs = 10 kHz
- Transformation ratio: n = 1:1
- Filtering capacitance on the PV side: Cpv = 3 mF
- Control: single phase shift (SPS) with a normalized phase ratio d ∈ [0, 0.5]

SPS control was chosen for its simplicity, robustness, and extensive validation [29] in high-power PV-battery applications; advanced modulations (EPS, DPS, and TPS) were beyond the scope of this study. This expression for the average DAB input current i_{dab1} [30], which is crucial for sizing components and optimizing converter control, PV input current, i_{pv}, split between filter capacitor current i_c and DAB input current, i_{dab1}, in (6).

$$i_{pv} = i_c + i_{dab1} \tag{6}$$

The DAB connects two active bridges via a leakage inductance transformer L with a ratio of n=1. Bridge 1 (PV source): input voltage V_{pv}, output V_1. Bridge 2 (battery): input voltage V_{bat}, output V_2. Voltages V_1 and V_2 generated by square signals s_1 and s_2, frequency $f_s = \frac{1}{T_s}$, phase shift $\tau = \frac{dT_s}{2}$, d in [0, 1] normalized, described in Figure 1. The inductance current i_L is governed by (7).

$$L\frac{di_L}{dt} = V_1 - V_2 \tag{7}$$

The SPS command generates four distinct phases within a period T_s, which is determined by the states of s_1 and s_2, as shown in Figure 5. These phases are described by (8)-(11).

$$i_L = \frac{1}{L}\int(V_{pv} + V_{bat})dt \quad (8)$$

$$i_L = \frac{1}{L}\int(V_{pv} - V_{bat})dt \quad (9)$$

$$i_L = \frac{1}{L}\int(-V_{pv} - V_{bat})dt \quad (10)$$

$$i_L = \frac{1}{L}\int(-V_{pv} + V_{bat})dt \quad (11)$$

The input current of bridge 1 is defined as follows (12):

$$i_{dab1} = s_1 i_L \quad (12)$$

The average value $< i_{dab1} >$ is calculated by exploiting the symmetry of the waveform and the integrals [31]; we obtain the expression (13), which will be simplified in (14).

$$< i_{dab1} > = \frac{V_{bat}}{2Lf} d(1 - |d|) \quad (13)$$

$$< i_{dab1} > = Du \quad (14)$$

Where $u = d(1 - |d|)$ captures the effect of the phase shift, and $D = \frac{V_{bat}}{2Lf}$ groups the system parameters.

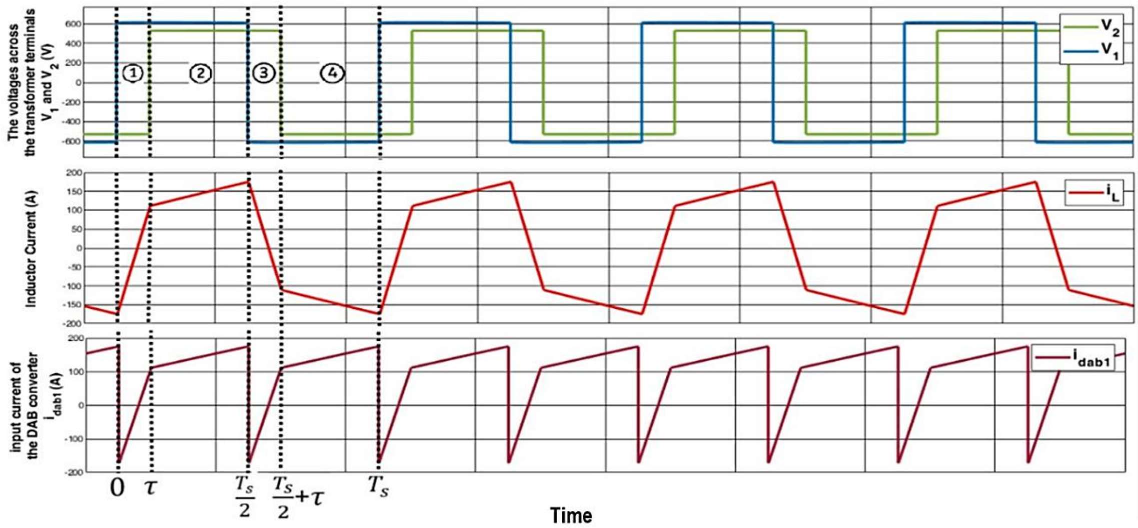

Figure 5. Four operating modes of the dual active bridge converter within one switching period Ts, determined by the states of bridges s1 and s2

2.2.3. PV-DAB-battery model

From the previously established average DAB model (14) and the physical model of the photovoltaic diode, a unique nonlinear dynamic equation for the average current ⟨iPV⟩ was derived. The assumptions made strong forward bias of the panel (Vpv ≫ VT) and slow climatic variations compared to the electrical dynamics of the converter (≥ 100 ms vs. ≤ 50 µs), which are widely validated in the literature for this type of application [23]. The hybrid approach presented in this section combines the two models to obtain an accurate and analytical representation of the complete system.

This section analyzes the average equation of C_{pv}, which is derived from the PV diode and the DAB circuit. To model the system, the impact of environmental variations should be assessed. The hybrid method combines the two models. First, derived from diode physics, simplifies (1) by assuming $i_d >>> i_0$ in forward bias, which results in (15).

$$V_d \approx \frac{nkT}{q} \ln\left(\frac{i_d}{i_0}\right) \tag{15}$$

Neglecting i_{rsh} as according to (1), we obtain (16), where i_{ph} depends on the irradiance G and temperature T. Its time derivative is expressed as (17).

$$i_d \approx i_{ph} - \frac{i_{pv}}{N_p} \tag{16}$$

$$\frac{di_{ph}}{dt} = \frac{i_{ph_0}}{1000}\left[\left(1 + \beta_T(T - 25)\right)\frac{dG}{dt} + \beta_T G \frac{dT}{dt}\right] \tag{17}$$

Taking the time derivative of (15) gives (18).

$$\frac{dV_d}{dt} = \frac{nkT}{q}\frac{1}{i_d}\frac{di_d}{dt} \tag{18}$$

Substituting the diode current expression (16) into (18) gives (19).

$$\frac{dV_d}{dt} = \frac{nkT}{q(N_p i_{ph} - i_{pv})}\left(N_p \frac{di_{ph}}{dt} - \frac{di_{pv}}{dt}\right) \tag{19}$$

Substituting (17) into (19) and expanding:

$$\frac{dV_d}{dt} = \frac{nkT}{q(N_p i_{ph} - i_{pv})}\left(\mathrm{N_p} \frac{i_{ph_0}}{1000}\left[\left(1 + \beta_T(T - 25)\right)\frac{dG}{dt} + \beta_T G \frac{dT}{dt}\right] - \frac{\mathrm{di_{pv}}}{\mathrm{dt}}\right) \tag{20}$$

Differentiating the resistive diode voltage expression (4) with respect to time yields the second expression for $\frac{dV_d}{dt}$:

$$\frac{dV_d}{dt} = \frac{1}{N_c N_s}\frac{dV_{pv}}{dt} + \frac{R_s}{N_c N_p}\frac{di_{pv}}{dt} \tag{21}$$

The (20), (21), and solving for $\frac{dV_{pv}}{dt}$, yields (22) with coefficients $\mathrm{A_3}, \mathrm{A_4},$ and $\mathrm{A_5}$ defined in (23)-(25).

$$\frac{dV_{pv}}{dt} = A_3 \frac{di_{pv}}{dt} + A_4 \frac{dG}{dt} + A_5 \frac{dT}{dt} \tag{22}$$

With:

$$A_3 = -\frac{nkTN_cN_s}{q(N_p i_{ph} - i_{pv})} - \frac{R_s N_s}{N_p} \tag{23}$$

$$A_4 = \frac{nkTN_cN_sN_p i_{ph_0}\left(1+\beta_T(T-25)\right)}{1000q(N_p i_{ph} - i_{pv})} \tag{24}$$

$$A_5 = \frac{nkTN_cN_sN_p i_{ph_0} G\beta_T}{1000q(N_p i_{ph} - i_{pv})} \tag{25}$$

This expression (26) is then substituted into the current conservation (6) in the average model. Hence, the term is expressed as (27).

$$i_{pv} = i_c + < i_{dab1} > \tag{26}$$

$$i_{pv} = C_{pv}\frac{dV_{pv}}{dt} + Du \tag{27}$$

Substituting (22) into (27), and identifying the coefficients, yields (28), where $f_1 = A_3 Cpv$, $f_2 = A_4 Cpv$ and $f_3 = A_5 Cpv$, defined in (29)-(31).

$$i_{pv} = Du + f_1(i_{pv}, G, T)\frac{di_{pv}}{dt} + f_2(i_{pv}, G, T)\frac{dG}{dt} + f_3(i_{pv}, G, T)\frac{dT}{dt} \quad (28)$$

Where:

$$f_1 = -Cpv\left(\frac{nkTN_cN_s}{q(N_pi_{ph}-i_{pv})} + \frac{R_sN_s}{N_p}\right) \quad (29)$$

$$f_2 = C_{pv}\left(\frac{nkTN_cN_sN_pi_{ph_0}(1+\beta_T(T-25))}{1000q(N_pi_{ph}-i_{pv})}\right) \quad (30)$$

$$f_3 = C_{pv}\frac{nkTN_cN_sN_pi_{ph_0}G\beta_T}{1000q(N_pi_{ph}-i_{pv})} \quad (31)$$

The analysis showed that f_1 acted as a dynamically stabilizing resistor. The terms f_2 and f_3, sensitive to G and T, integrate thermal and geometric effects essential to adaptive MPPTs. The common dependence on this equation highlights the importance of forward bias. This equation allows for the simulation of transients (e.g., cloud passage) and the design of C_{pv} of an efficient filtration.

2.3. Design and implementation of gain-scheduled PI controller for PV-DAB-battery system

Unlike conventional fixed-gain PI controllers which assume constant dynamics, f_1 varies significantly with the operating point. Figure 6 illustrates the variation of the time constant $f_1(ipv, G, T)$ as a function of irradiance G and PV current ipv at T = 25 °C. However, regardless of operating conditions, f_1 is analytically bounded by ($f_1 < -Cpv\frac{R_sN_s}{N_p} = -1.575ms$ in our system).

Since for all physical operating conditions (G>0, T>0K, $N_pi_{ph} > i_{pv}$), the term $\frac{nkTN_cN_s}{q(N_pi_{ph}-i_{pv})} > 0$ always. This variation off_1 is precisely the motivation for the proposed gain-scheduling approach: the gains k_p and k_i are recalculated at each 1 µs sample via (41) and (42) to compensate for this nonlinearity and maintain constant closed-loop dynamics.

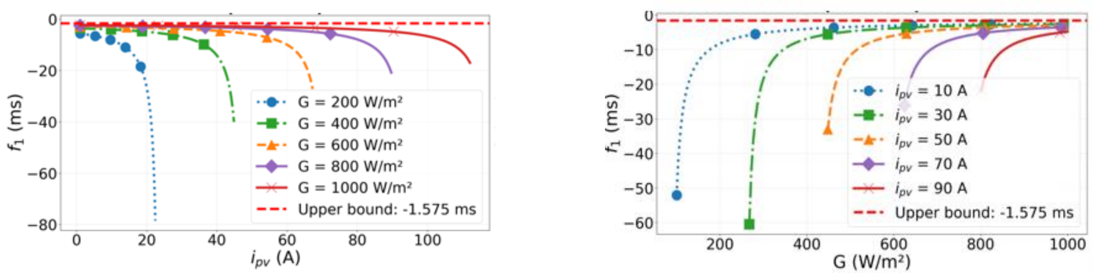

Figure 6. Time constant f_1 variation under T=25 °C: (a) f_1 vs. i_{pv} for different G values and (b) f_1 vs. G for different i_{pv} values

The nonlinear dynamics of the system in (28)-(31) are locally linearized around the instantaneous operating point. All control calculations (Kp, Ki gain adjustment, anticipation disturbance compensation, saturation protection, and phase-shift saturation) were performed every 1 us (1 MHz control frequency). This extremely high sampling frequency is necessary because the assumption of local linearity and the discrete time simplifications remain valid only if the PV voltage and current are considered quasi-constant over a DAB switching cycle (10 µs). Such a precise control step ensures second-order closed-loop behavior and excellent disturbance rejection, even with rapid irradiance changes, without compromising the numerical accuracy [32].

Dynamic modeling of the PV-DAB system (28) leads to the design of a gain-scheduled PI controller and disturbance compensation, ensuring precise tracking of i_{pv} towards i_{pvref}, despite variations in G and T. The basic system, without disturbances, is modelled as (32).

$$i_{pv} = Du + f_1(i_{pv}, G, T)\frac{di_{pv}}{dt} \quad (32)$$

The perturbing terms $f_2 \frac{dG}{dt}$ and $f_3 \frac{dT}{dt}$ are compensated separately. The key assumption is that $T_e = 1\ us$ is sufficiently small compared to the system dynamics (typically milliseconds); this small scale allows us to use the Taylor approximation to estimate the variations of quantities on T_e. The Taylor series of $f_i(t_k + T_e)$ around t_k is expressed as:

$$f_i(t_k + T_e) \approx f_i(t_k) + \frac{df_i}{dt}(t_k) \times T_e, \tag{33}$$

with $T_e = 1\ \mu s$, and assuming slow dynamics (e.g. $\frac{df_i}{dt}(t_k) \times T_e$) of the order of 10^{-4}, then:

$$f_i(t_k + T_e) \approx f_i(t_k) \tag{34}$$

This approximation facilitates quasi-continuous analysis, although numerical validation is required to confirm its robustness against fast perturbations. Similarly, in the same way we can neglect the variations of G and T in a sample. The last approximation is necessary for calculating the compensation command. Moreover, this hypothesis is based on the local linearity.

The control strategy combines a classical PI controller (35), where e is the error (36), considering the compensation term (37) that provides total control (38).

$$u_{pi} = k_p e + \int (k_i e) dt \tag{35}$$

$$e = i_{pvref} - i_{pv}, \tag{36}$$

$$u_{comp} = -\frac{1}{D}\left(f_2(i_{pv}, G, T)\frac{dG}{dt} + f_3(i_{pv}, G, T)\frac{dT}{dt}\right) \tag{37}$$

$$u = u_{pi} + u_{comp} \tag{38}$$

This separation handles the main regulation via PI and cancels the external effects via u_{comp}. The gains k_p and k_i are derived to align the response to a second-order system with a natural frequency ω_n and damping factor ξ. The closed-loop transfer function is given by (39).

$$T(s) = \frac{Dk_p s + Dk_i}{-f_1 s^2 + (1 + Dk_p)s + Dk_i} \tag{39}$$

The stability of the proposed controller is inherent to its structure: rather than stabilizing an unstable system, the gain-scheduling law enforces a desired second-order behavior whose stability is guaranteed by construction. The closed-loop poles are analytically imposed at each sampling instant as (40).

$$s_{1,2} = -\xi\omega_n \pm \omega_n\sqrt{\xi^2 - 1} \tag{40}$$

For any $\xi>0$ and $\omega_n>0$, the real part of the poles is strictly negative, guaranteeing closed-loop stability regardless of the operating point. By identification with the standard second-order system, the gains k_p and k_i are derived as (41) and (42).

$$k_i = \frac{-f_1\omega_n^2}{D} \tag{41}$$

$$k_p = -\frac{1 + 2\xi\omega_n f_1}{D} \tag{42}$$

To maintain second-order dynamics despite variations in f_1 (related to i_{pv}, G, T), ω_n and ξ are fixed, and the gains are recalculated, preserving the transient response. The transfer function (39) also contains a zero at $-\frac{k_i}{k_p} = \frac{-f_1\omega_n^2}{1+2\xi\omega_n f_1}$. Since $-f_1\omega_n^2 > 0$ always, the sign of z depends on the denominator $1 + 2\xi\omega_n f_1$. A left-half-plane zero (z<0) is essential to ensure minimum-phase behavior: a right-half-plane zero (z>0) would cause an undershoot in the step response. From the analytical bound $f_1 < -Cpv\frac{R_S N_S}{N_p}$ the denominator satisfies $1 + 2\xi\omega_n f_1<0$, and therefore z<0, provided that:

$$\xi\omega_n > \frac{N_p}{2C_{pv}R_S N_S} \tag{43}$$

Figure 7 illustrates this guaranteed minimum-phase region in the ($\xi\omega_n$) design space. All three simulation cases are well within this region, confirming that the closed-loop zero remains strictly in the left-half-plane across the entire operating range, regardless of G, T, and ipv. This flowchart presents the Gain-Scheduled PI control algorithm (Figure 8) for our systems. It calculates the phase ratio (d) from the inputs (current, irradiance, temperature), integrating the error, PI output, compensation, and control signal limitations.

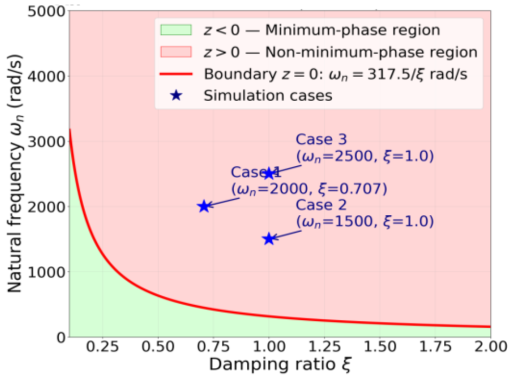

Figure 7. Guaranteed minimum-phase region (z<0) in the (ξ, ωn) design space; all three simulation cases lie within the valid region, confirming left-half-plane zero placement across the full operating range

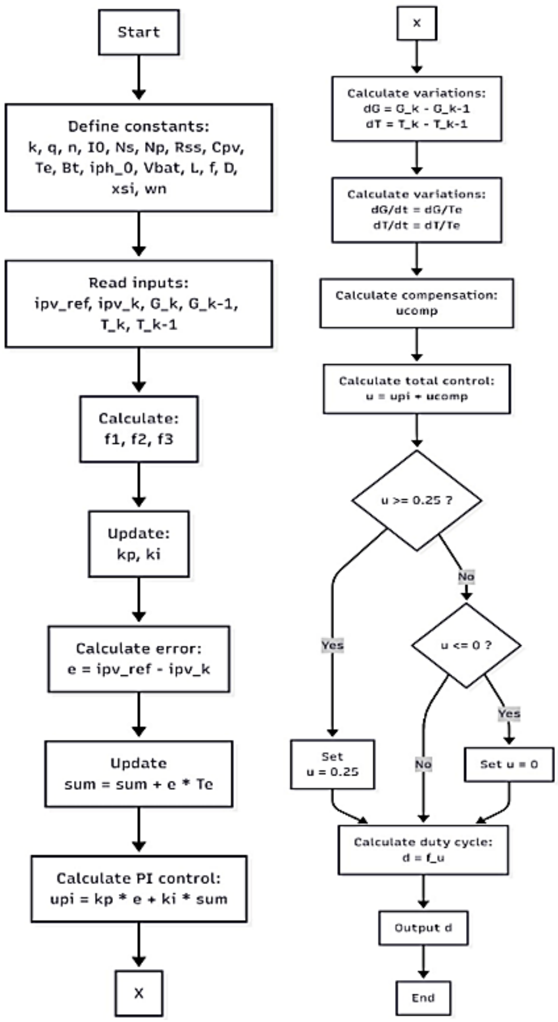

Figure 8. Flowchart of the gain-scheduled PI control algorithm

3. RESULTS AND DISCUSSION

3.1. Regulation with fixed setpoint and variations of G

Figure 9 shows the irradiance profile specifically designed to reproduce real conditions: a constant plateau of 1000 W/m² from 0 to 1 s, followed by a smooth linear ramp of exactly one second descending to 700 W/m², simulating the typical passage of a partial cloud, and then a constant maintenance at 700 W/m² up to 3 s. The cell temperature was maintained at 25 °C according to standard test conditions (STC) throughout this test scenario in order to isolate the effect of irradiance variations and allow direct comparison with manufacturer datasheet values.

A current setpoint step from 0 to 70 A was applied at t = 5 ms (Te = 1 µs). Figures 9 to 11 compare: i) A conventional fixed-gain PI controller using the converged gains of the proposed controller in the stabilized state under 1000 W/m² (Kp= 3.775 × 10^{-3}; Ki =7.22), and ii) the proposed analytical gain-scheduled controller ($\xi = 1$, $\omega_n = 2500$ rad/s). Table 2 summarizes the measured performance as presented in Figure 10. During the irradiance ramp (1000 → 700 W/m² in 1 s), the two correctors exhibited a transient error of the same maximum amplitude (≈ 1 A), which was expected because both temporarily saturated the D control at 0.25.

Figure 11 shows that the Kp and Ki gains of the proposed corrector adapt automatically during the ramp-down (Kp changes from ≈ 3.8 × 10^{-3} to ≈ 12.65× 10^{-3} and Ki from ≈ 7.2 to ≈ 18.3 when switching from 1000 to 700 W/m²), and then stabilize at their new optimal values as soon as the irradiance becomes constant at 700 W/m². This real-time adaptation is precisely the function of analytical gain scheduling. These results demonstrate that, even though a classic PI set with optimal gains at 1000 W/m² presents a more aggressive response than the proposed method. Conversely, only the proposed analytical gain-scheduled controller guarantees the following: i) negligible overshoot and absence of oscillations dependent on the desired behavior (no oscillation in our case), and ii) an overall response time three times shorter (0.94 ms versus 2.94 ms at ±5%).

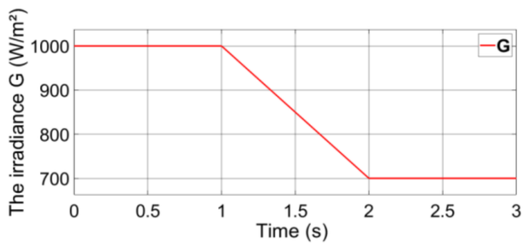

Figure 9. Irradiance variations G applied to the system

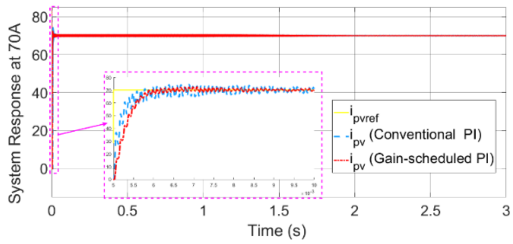

Figure 10. Time-domain response comparison of gain-scheduled and conventional PI controllers to a 70 A setpoint

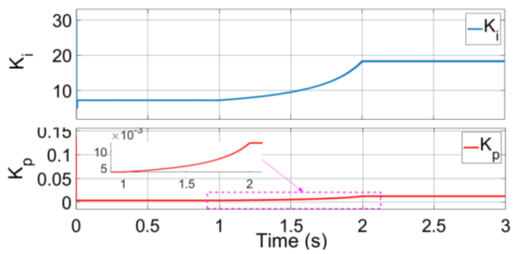

Figure 11. Temporal adaptation of proportional (k_p) and integral (k_i) gains

Table 2. Transient performance

Indicator	Classical PI (extracted gains)	Gain-scheduled proposed	Noticed
Response time to ±5% (step)	2.94 ms	0.94 ms	3.1 times faster and perfectly stable
Overshoot (level)	>6.5%	≈1%	—
Rise time 10% → 90% (5 ms increments)	0.353 ms	0.650 ms	Classic PI is faster due to overshoot

Note: Kp and Ki fixed gains extracted from the proposed controller at steady state under G = 1000 W/m², T = 25 °C. Response times measured at ±5% of the 70 A setpoint.

3.2. Performance dependence on operating points

To irrefutably demonstrate the intrinsic limitation of a fixed-gain PI on a strongly nonlinear process, two very different current setpoints were imposed at constant irradiance and temperature (G = 1000 W/m², T = 25 °C): 70 A from 0 to 0.1 s, followed by a sudden jump to 100 A at t = 0.1 s. The results are presented in Figure 12 and Table 3. Figure 12 clearly shows that the conventional PI controller, even when optimally set to 70 A, becomes highly oscillatory (oscillations with an amplitude >6.5% for almost 28 ms) as soon as the setpoint increases to 100 A.

Conversely, the proposed gain-scheduled controller maintains the same response quality at both operating points: i) nearly identical rise time (0.57–0.65 ms), ii) overall response time was always less than 1.1 ms, and iii) negligible overshoot and absence of oscillations. This comparison constitutes strong simulation evidence: only the proposed analytical gain scheduling is capable of maintaining a fast, strictly critical ($\xi = 1$), and perfectly stable dynamic over the entire current setpoint range. In contrast, the PI controller with fixed gains systematically becomes oscillatory or excessively slow when operating away from the tuning point.

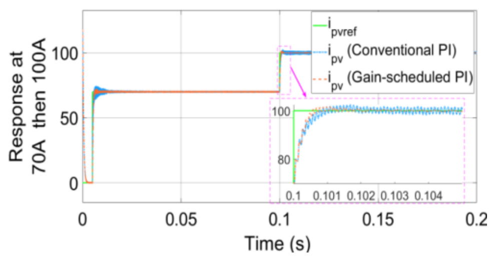

Figure 12. Comparison of the performance of the two controllers for two different current setpoints (70 A and 100 A)

Table 3. Performance during the setpoint jump from 70 A to 100 A

Target	Corrector	Response time to ±5% (step)	Rise time 10% → 90% (5 ms increments)	Overshoot
70 A	Classic PI (gains fixed for 70 A)	0.353 ms	2.94 ms	>6.5%
70 A	Proposed gain-scheduled ($\omega_n = 2500$, $\xi = 1$)	0.650 ms	0.94 ms	≈1%
100 A	Classic PI (gains fixed for 70 A)	0.680 ms	27.83 ms	>6.66%
100 A	Proposed gain-scheduled ($\omega_n = 2500$, $\xi = 1$)	0.570 ms	1.085 ms	≈1%

Note: Fixed PI gains optimized for 70 A setpoint only. The proposed controller maintains identical specifications ($\xi = 1$, $\omega n = 2500$ rad/s) at both operating points.

3.3. Influence of the choice of closed-loop specifications (ω_n, ξ)

To verify that the proposed method imposes the specified second-order dynamics, regardless of operating conditions, three different sets of specifications were tested with fixed irradiance and temperature (G = 1000 W/m², T = 25 °C) and a constant current setpoint of 70 A (Figure 13). Figure 13 shows that the second-order dynamics were respected in all three cases. The overshoot measured at $\xi = 0.707$ (8.25%) is slightly higher than the pure theoretical value of a linear second-order system (4.32%), owing to the temporary saturation of control D at its maximum value (0.25) during the initial moments of the rise. This saturation, which is unavoidable during a sudden 70 A step, introduces a transient nonlinearity that slightly increases the actual overshoot while maintaining an overall response that conforms to the specification.

Table 4 presents the performance indicators measured for the three sets of specifications (ω_n, ξ) applied to the proposed gain-scheduled controller. These results confirm the validity of the analytical expressions for the gains Kp and Ki in (41) and (42). They also demonstrate that the user can freely choose the speed (via ω_n) and damping rate (via ξ) of the closed loop, while the method rigorously imposes the specified dynamics even in the presence of physical saturation of the converter.

Table 4. Influence of closed-loop specifications (setpoint 70 A)

Case	ω_n (rad/s)	ξ	Rise time 10% → 90% (5 ms increments)	95 % response time	Overshoot observed	Theoretical overshoot
Underdamped	2000	0.707	0.78 ms	1.47 ms	8.25%	4.32%
Critically damped	1500	1.0	1.18 ms	1.92 ms	0%	0%
Critically damped	2500	1.0	0.61 ms	0.94 ms	0%	0%

Note: Overshoot at $\xi = 0.707$ exceeds theoretical value (4.32%) due to transient saturation of control variable d at its maximum (0.25) during the initial rise.

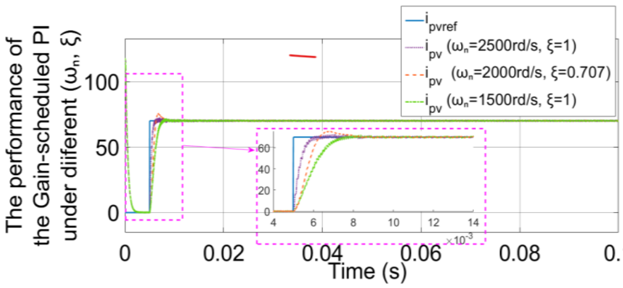

Figure 13. Influence of the choice of closed loop specifications (ω_n, ξ) on the performance of the PI with programmed gains and perturbation compensation

3.4. MPPT test under environmental variations

Figure 14 shows the development of the PV current ipv(t) to obtain the MPP under a realistic irradiance profile: fixed irradiance at 400 W/m² (0–1 s), smooth 1-second ramp to 800 W/m² (1–2 s), then fixed irradiance at 800 W/m² (2–3 s). The current setpoint ipv_ref was generated in real time by the neural network published in our previous article [33], and its MPPT performance has already been experimentally validated. At the start-up (t = 0, G = 400 W/m²), the proposed gain-scheduled correction exhibited significantly superior dynamics (faster rise without overshoot or oscillation). During the irradiance ramp (400 → 800 W/m²), the gain-scheduled controller closely followed the ipv_ref setpoint generated by the neural network owing to the automatic adaptation of the Kp and Ki gains, rigorously maintaining the specified critical dynamic range (ξ = 1, ω_n = 2500 rad/s). The conventional PI controller exhibited a slight delay and small residual oscillations.

Figure 15 shows the PV power Ppv (t) extracted by the two controllers. The precise tracking of the MPP is evident: both Ppv curves remain very close to the theoretical maximum power, with a slight transient advantage for the gain-scheduled controller during the ramp-up phase. Figure 16 shows the instantaneous power difference ΔP = P_gain-scheduled – P_PI-classic.

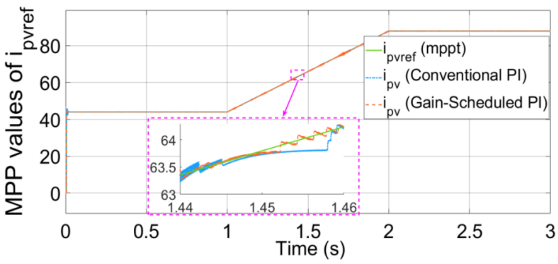

Figure 14. PV current ipv(t) under realistic irradiance variation (400 W/m² → 800 W/m²)

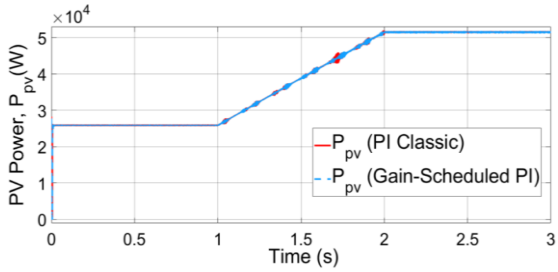

Figure 15. Extracted PV power Ppv(t) under realistic irradiance variation (400 → 800 W/m²)

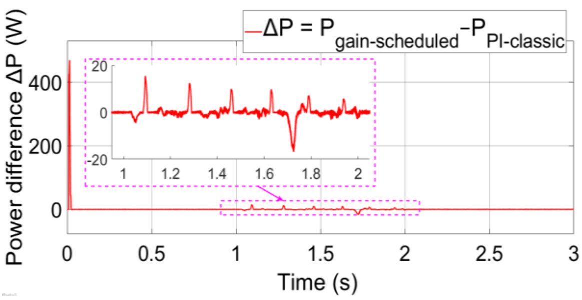

Figure 16. Instantaneous power difference ΔP = P_gain-scheduled − P_PI-classic under realistic irradiance profile (400→800 W/m²), showing a consistently positive energy advantage for the proposed controller

This difference was mostly positive at startup and during the irradiance ramp, reflecting a transient energy gain in favor of the proposed corrector. Throughout the entire test, the net energy gain remained positive for the proposed corrector, with a slightly higher average power (+0.4%). These results demonstrate that the combination of the validated neural network for the generation of ipv_ref and the proposed analytical gain-scheduled corrector makes it possible to obtain a fast, robust, and stable full MPPT, with perfectly controlled dynamics over the entire operating range, and a performance superior to that of a classic PI with fixed gains, even under conditions of slow variation.

4. CONCLUSION

This study proposes an innovative adaptive control strategy for MPPT in a PV-battery system based on a DAB converter. The gain-scheduled PI controller, with gains recalculated every 1 μs by local linearization of the nonlinear model and explicit compensation of disturbances (derivatives of G and T), imposes a constant second-order dynamic (response time ≈ 1 ms, $\xi = 1$) over the entire operating range. Simulations under realistic irradiance profiles showed a clear superiority over a classic PI with fixed gains: elimination of oscillations and significant reduction of overshoot, reduced response time by a factor greater than 3, stable performance despite large variations in the operating point, and a transient energy gain of 0.4% during cloud passage events, collectively improving battery lifetime and system reliability. To the best of our knowledge, this gain-scheduled analytical approach with explicit disturbance compensation has not been developed for the DAB topology in PV-battery systems. It is distinguished by its simplicity (≈ 180–200 floating-point operations per 1 μs sample, executable on standard DSPs), without requiring additional state observers, and predictable performance without complex observers.

Several limitations should be acknowledged. First, the controller assumes ideal real-time measurement of the derivatives of G and T, which may be affected by sensor noise in practical deployments. Second, the 1 μs sampling frequency, while numerically validated here, requires careful DSP selection for real-time implementation, as it imposes a processing budget of approximately 180–200 floating-point operations per cycle — feasible on high-performance DSPs (e.g., TMS320F28379D) but constraining on lower-cost platforms. Third, the current formulation targets a single PV-DAB-battery port; extension to multi-source hybrid systems (e.g., PV-wind-battery) would require reformulation of the gain-scheduling law to account for inter-port coupling dynamics. Experimental validation on a prototype is planned at the Information Processing Laboratory (FS Ben M'Sick). Ultimately, this control opens up possibilities for multi-source systems, the management of parametric uncertainties, and hybridization with AI for MPPT under partial shading, contributing to more robust and accessible renewable-energy systems.

FUNDING INFORMATION

The authors state that no funding was involved in this study.

AUTHOR CONTRIBUTIONS STATEMENT

This journal uses the Contributor Roles Taxonomy (CRediT) to recognize individual author contributions, reduce authorship disputes, and facilitate collaboration.

Name of Author	C	M	So	Va	Fo	I	R	D	O	E	Vi	Su	P	Fu
Khalid Sabhi	✓	✓	✓	✓	✓	✓		✓	✓	✓				✓
Mohamed Talea				✓		✓	✓			✓	✓	✓	✓	
Hicham Bahri	✓			✓				✓		✓	✓		✓	

C : **C**onceptualization
M : **M**ethodology
So : **So**ftware
Va : **Va**lidation
Fo : **Fo**rmal analysis
I : **I**nvestigation
R : **R**esources
D : **D**ata Curation
O : Writing - **O**riginal Draft
E : Writing - Review & **E**diting
Vi : **Vi**sualization
Su : **Su**pervision
P : **P**roject administration
Fu : **Fu**nding acquisition

CONFLICT OF INTEREST STATEMENT

Authors state no conflict of interest.

DATA AVAILABILITY

Data availability is not applicable to this paper as no new data were created or analyzed in this study.

REFERENCES

[1] A. E. Lawin, M. Niyongendako, and C. Manirakiza, "Solar irradiance and temperature variability and projected trends analysis in Burundi," *Climate*, vol. 7, no. 6, p. 83, Jun. 2019, doi: 10.3390/cli7060083.

[2] G. Modi and B. Singh, "Power quality improvement in solar energy conversion system integrated to weak AC grid," *Journal of The Institution of Engineers (India): Series B*, vol. 105, no. 6, pp. 1511–1526, Dec. 2024, doi: 10.1007/s40031-024-01046-7.

[3] A. Guerbouz, I. Merzouk, A. Hfaifa, and A. Fihakhir, "Photovoltaic MPPT control using SEPIC converter based on super twisting control," *The Scientific Bulletin of Electrical Engineering Faculty*, vol. 24, no. 2, pp. 22–29, Dec. 2024, doi: 10.2478/sbeef-2024-0017.

[4] M. L. Katche, A. B. Makokha, S. O. Zachary, and M. S. Adaramola, "A comprehensive review of maximum power point tracking (MPPT) techniques used in solar PV systems," *Energies*, vol. 16, no. 5, p. 2206, Feb. 2023, doi: 10.3390/en16052206.

[5] L. El Oussoul, A. Elhamdaouy, and A. Ait Madi, "A new MPPT control strategy based on a weighting mechanism: enhancing efficiency in solar energy harvesting," *Results in Engineering*, vol. 26, p. 104725, Jun. 2025, doi: 10.1016/j.rineng.2025.104725.

[6] U. Siddaraj, U. R. Yaragatti, L. R. S. Paragonda, and S. Tangi, "Adaptive MPPT control for reliable transitions between grid connected and islanded operations in PV battery microgrids," *Scientific Reports*, vol. 16, no. 1, p. 7613, Feb. 2026, doi: 10.1038/s41598-026-38300-5.

[7] Y. R. Sankar and K. C. Sekhar, "Hybrid PV/fuel cell based system using integrated SEPIC-Cuk converter with crow search optimized PI controller," *International Journal of Power Electronics and Drive Systems (IJPEDS)*, vol. 15, no. 3, p. 1726, Sep. 2024, doi: 10.11591/ijpeds.v15.i3.pp1726-1738.

[8] S. Shi, J. Du, B. Xia, D. Xia, H. Guan, and F. Wang, "Research on optimum extended phase-shift control with minimum peak-to-peak current of DAB converter applied to small DC power grid," *Frontiers in Energy Research*, vol. 10, Jan. 2023, doi: 10.3389/fenrg.2022.1115146.

[9] H. Ataullah *et al.*, "Analysis of the dual active bridge-based DC-DC converter topologies, high-frequency transformer, and control techniques," *Energies*, vol. 15, no. 23, p. 8944, Nov. 2022, doi: 10.3390/en15238944.

[10] J. A. González-Castro *et al.*, "Integrated sliding mode control and adaptive-step P&O MPPT strategy for DC–DC boost–buck converter in photovoltaic systems," *Energies*, vol. 19, no. 5, p. 1123, Feb. 2026, doi: 10.3390/en19051123.

[11] H. Kotb, A. G. Khairalla, H. B. ElRefaie, and K. M. AboRas, "Enhanced power management in PV-Integrated hybrid energy storage systems using fuzzy 2DOF-PI control optimized by hippopotamus algorithm," *Scientific Reports*, vol. 16, no. 1, p. 9200, Mar. 2026, doi: 10.1038/s41598-026-40106-4.

[12] S. Kurm and V. Agarwal, "Dual active bridge based reduced stage multiport DC/AC converter for PV-battery systems," *IEEE Transactions on Industry Applications*, vol. 58, no. 2, pp. 2341–2351, Mar. 2022, doi: 10.1109/TIA.2021.3137371.

[13] M. Jafari and Z. Malekjamshidi, "A hybrid renewable energy system integrating photovoltaic panels, wind turbine, and battery energies for supplying a grid-connected residential load," *SN Applied Sciences*, vol. 2, no. 11, p. 1852, Nov. 2020, doi: 10.1007/s42452-020-03654-6.

[14] T. Hai, J. Zhou, and N. Furukawa, "Performance enhancement of fuzzy-PID controller for MPPT of PV system to extract maximum power under different conditions," *Soft Computing*, vol. 28, no. 3, pp. 2035–2054, Feb. 2024, doi: 10.1007/s00500-023-09171-z.

[15] T. N. Olayiwola, S.-H. Hyun, and S.-J. Choi, "Photovoltaic modeling: a comprehensive analysis of the I–V characteristic curve," *Sustainability*, vol. 16, no. 1, p. 432, Jan. 2024, doi: 10.3390/su16010432.

[16] A. Das and S. Peu, "Modeling of PV cell, PV module, PV array and PV IV characteristics analysis using MATLAB/SIMULINK," Sep. 20, 2022, doi: 10.20944/preprints202209.0304.v1.

[17] A. Alhejji and M. I. Mosaad, "Performance enhancement of grid-connected PV systems using adaptive reference PI controller," *Ain Shams Engineering Journal*, vol. 12, no. 1, pp. 541–554, Mar. 2021, doi: 10.1016/j.asej.2020.08.006.

[18] B. Mahbouba, M. Afef, H. Hichem, B. R. Chiheb, and Z. Abderrahmen, "A novel MPPT algorithm based on MRAC-FUZZY controller for solar photovoltaic systems," *Power Electronics and Drives*, vol. 10, no. 1, pp. 140–156, Jan. 2025, doi: 10.2478/pead-2025-0011.

[19] J. Maddikari and D. K. Das, "Design of an adaptive auto-tuned proportional-integral (PI) adaptive MPPT controller for a solar photovoltaic system," Jul. 14, 2023, doi: 10.21203/rs.3.rs-3155984/v1.

[20] T.-Q. Duong, H.-A. Trinh, K.-K. Ahn, and S.-J. Choi, "Adaptive extended state observer for the dual active bridge converters," *Sensors*, vol. 24, no. 8, p. 2397, Apr. 2024, doi: 10.3390/s24082397.

[21] X. Li, X. Zhang, F. Lin, C. Sun, and K. Mao, "Artificial-intelligence-based triple phase shift modulation for dual active bridge converter with minimized current stress," *IEEE Journal of Emerging and Selected Topics in Power Electronics*, vol. 11, no. 4, pp. 4430–4441, Aug. 2023, doi: 10.1109/JESTPE.2021.3105522.

[22] E. Hosseini *et al.*, "Optimal energy management system for grid-connected hybrid power plant and battery integrated into multilevel configuration," *Energy*, vol. 294, p. 130765, May 2024, doi: 10.1016/j.energy.2024.130765.

[23] E. E. Henao-Bravo, C. A. Ramos-Paja, and A. J. Saavedra-Montes, "Adaptive control of photovoltaic systems based on dual active bridge converters," *Computation*, vol. 10, no. 6, p. 89, Jun. 2022, doi: 10.3390/computation10060089.

[24] E. E. Henao-Bravo, C. A. Ramos-Paja, A. J. Saavedra-Montes, D. González-Montoya, and J. Sierra-Pérez, "Design method of dual active bridge converters for photovoltaic systems with high voltage gain," *Energies*, vol. 13, no. 7, p. 1711, Apr. 2020, doi: 10.3390/en13071711.

[25] M. F. Fiaz, S. Calligaro, M. Iurich, and R. Petrella, "Analytical modeling and control of dual active bridge converter considering all phase-shifts," *Energies*, vol. 15, no. 8, p. 2720, Apr. 2022, doi: 10.3390/en15082720.

[26] I. A. Razzhivin, A. A. Suvorov, R. A. Ufa, M. V. Andreev, and A. B. Askarov, "The energy storage mathematical models for simulation and comprehensive analysis of power system dynamics: a review. Part I," *International Journal of Hydrogen Energy*, vol. 48, no. 58, pp. 22141–22160, Jul. 2023, doi: 10.1016/j.ijhydene.2023.03.070.

[27] I. A. Razzhivin, A. A. Suvorov, R. A. Ufa, M. V. Andreev, and A. B. Askarov, "The energy storage mathematical models for simulation and comprehensive analysis of power system dynamics: a review. Part II," *International Journal of Hydrogen Energy*, vol. 48, no. 15, pp. 6034–6055, Feb. 2023, doi: 10.1016/j.ijhydene.2022.11.102.

[28] M. H. M. Hariri, M. Salem, M. K. M. Jamil, M. N. Abdullah, and M. K. M. Desa, "Modeling and analysis of 100 kW two-stage three-phase grid-connected PV generation system under absurd atmospheric and grid disturbances," *PLOS One*, vol. 20, no. 6, p. e0323269, Jun. 2025, doi: 10.1371/journal.pone.0323269.
[29] S. Kuo *et al.*, "High efficiency dual-active-bridge converter with triple-phase-shift control for battery charger of electric vehicles," *Energies*, vol. 17, no. 2, p. 354, Jan. 2024, doi: 10.3390/en17020354.
[30] D. A. Herrera-Jaramillo, E. E. Henao-Bravo, D. G. Montoya, C. A. Ramos-Paja, and A. J. Saavedra-Montes, "Control-oriented model of photovoltaic systems based on a dual active bridge converter," *Sustainability*, vol. 13, no. 14, p. 7689, Jul. 2021, doi: 10.3390/su13147689.
[31] G. D. Sukumar, R. R. Prasad, R. H. Vardhan, B. Pakkiraiah, and C. L. Krishna, "Fuzzy controlled MPPT to grid connected PV systems," *E3S Web of Conferences*, vol. 616, p. 01010, Feb. 2025, doi: 10.1051/e3sconf/202561601010.
[32] A. Alemanno, R. Morici, M. Pretelli, and C. Florian, "Design of a 7.5 kW Dual active bridge converter in 650 V GaN technology for charging applications," *Electronics*, vol. 12, no. 6, p. 1280, Mar. 2023, doi: 10.3390/electronics12061280.
[33] K. Sabhi, M. Talea, H. Bahri, and S. Dani, "Integrating dual active bridge DC-DC converters: a novel energy management approach for hybrid renewable energy systems," *Electrical Engineering & Electromechanics*, no. 2, pp. 39–47, Mar. 2025, doi: 10.20998/2074-272X.2025.2.06.

BIOGRAPHIES OF AUTHORS

Khalid Sabhi was born in Morocco in 1990. He is a Ph.D. student at the Laboratory of Information Processing, FSBM Casablanca, Hassan 2 University in Morocco. In 2014, he graduated with honors from Morocco's Faculty of Science and Technology of FES with a degree in mechatronic engineering. His research activities include the design, control, and intelligent management of renewable hybrid energy systems. He can be contacted at email: sabhi.khalid.imt@gmail.com.

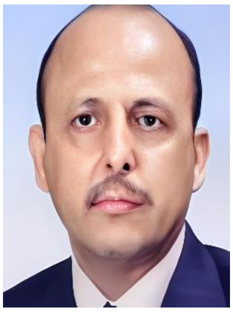

Mohamed Talea received his Ph.D. degree in physics in collaboration with Poitiers University, France, in 2001. He obtained a doctorate of high graduate studies degree from Hassan II University, Morocco, in 1994. Currently, he is a professor in the Department of Physics at Hassan II University, Morocco, and he is the director of the Laboratory of Information Processing. He can be contacted at email: taleamohamed@yahoo.fr.

Hicham Bahri received a master's degree in automatic at Science and Techniques Faculty, from University Hassan I, in Settat, Morocco, in 2014. In 2019, he received his Ph.D. in "Elaboration of an advanced control strategy of three phase grid connected photovoltaic system" in the Laboratory of System Analysis and Information Processing from University Hassan I. He is currently a professor in Physics Department at Faculty of Science Ben M'Sik, University Hassan II Casablanca, Morocco. His research in Information Treatment Laboratory consists in the control of the linear and nonlinear systems with use of the advanced controller and he is an expert in IT development. He can be contacted at email: hbahri.inf@gmail.com.